Materials Advances

ROYAL SOCIETY OF CHEMISTRY

PAPER

View Article Online
View Journal | View Issue

Cite this: *Mater. Adv.*, 2024, 5, 6270

Inkjet-printed Ce-doped SnO_x electron transport layer for improved performance of planar perovskite solar cells†

Dongli Lu, [a] Mahboubeh Jamshidi, [b] Chaochao Dun, [c] Jeffrey J. Urban, [c] James M. Gardner [b] and Liubov Belova*[a]

Planar perovskite solar cells (PSCs) based on low-temperature solution-processed SnO_2 electron transport layers (ETLs) usually suffer from energy losses within SnO_2 ETLs or at SnO_2/perovskite interfaces. Doping is an effective strategy to modify the properties of SnO_2 and reduce such energy losses. Herein, Ce ions are incorporated into solution-processed SnO_x and Ce-doped SnO_x ETLs are fabricated for planar PSCs *via* inkjet printing. The Ce-doped SnO_x ETL shows enhanced conductivity and improved energy level alignment with the perovskite layer, which can facilitate charge extraction and transport capabilities. Ce doping also effectively passivates the surface defects of SnO_x. The photoluminescence characterization reveals that the carrier recombination is suppressed within the perovskite film. As a result, an improved power conversion efficiency (PCE) of 15.77% is obtained for the planar PSC with a Ce-doped SnO_x ETL, compared to that of 14.66% for the undoped device. Furthermore, this work demonstrates a sustainable fabrication method which has great potential for the upscaling of PSCs.

Received 31st January 2024,
Accepted 21st June 2024

DOI: 10.1039/d4ma00094c

rsc.li/materials-advances

Introduction

Tin oxide (SnO_2) has been utilized as an effective electron transport layer (ETL) for perovskite solar cells (PSCs) because of its high mobility, chemical and optical stability, and favorable energy band alignment with perovskite.[1,2] The feasibility of low-temperature solution fabrication process makes it compatible with roll-to-roll production processes and flexible PSCs.[3] However, low-temperature solution-processed SnO_2 is prone to suffering from defects and high electron transport resistance at ETL/perovskite interfaces within planar PSCs.[4,5] To date, one of the strategies for improving power conversion efficiency (PCE) and stability of SnO_2 based PSCs is to reduce energy losses within SnO_2 ETLs or at ETL/perovskite interfaces, *i.e.*, modifying the properties of SnO_2 and passivating the ETL/perovskite interfaces.[6]

Doping of SnO_2 is a commonly used approach to adjust the properties of SnO_2 and is easily compatible with a low-temperature solution processing. Metal-ion doping (*e.g.*, Zn, Al, La, Cu, Ga, Y, Sb, and Li) can usually improve the electronic properties of SnO_2, such as enhancing the conductivity and enabling a better energy level alignment with perovskite, which facilitates the electron extraction and transport capability and inhibits charge recombination, leading to improved PCE and stability.[7–15] For example, Wang *et al.* doped SnO_2 with gadolinium ions, which passivated oxygen defects at the SnO_2 surface and optimized the energy level matching between the SnO_2 ETL and the perovskite layer, and thus achieved an improved PCE with a reduced hysteresis.[16] Ren *et al.* reported that the low-temperature solution-processed Nb-doped SnO_2 ETL outperformed the pristine SnO_2 ETL, originating from improved surface morphology, higher electron mobility, larger electrical conductivity, and enhanced electron extraction.[17] Zirconium doping upshifted the energy levels of SnO_2 and Zr-doped SnO_2 showed improved alignment of the conduction band maximum (E_{CBM}) with perovskite layers, in combination with enhanced conductivity and decreased surface defect density, which improved the electron extraction/transport properties, increased the carrier lifetime, and suppressed the charge recombination rate, contributing to the improved PCE of PSCs with marginal hysteresis.[18] In addition, organic or inorganic compounds as functional materials were doped or introduced into SnO_2 ETLs, such as sulfur-doped graphite carbon nitride,[19] 3-(formamidinothio)-1-propanesulfonic acid,[20] black phosphorus quantum

[a] *Department of Materials Science and Engineering, KTH Royal Institute of Technology, 10044 Stockholm, Sweden. E-mail: lyuba@kth.se*
[b] *Department of Chemistry, Applied Physical Chemistry, KTH Royal Institute of Technology, 10044 Stockholm, Sweden*
[c] *The Molecular Foundry, Lawrence Berkeley National Laboratory, Berkeley, CA 94720, USA*

† Electronic supplementary information (ESI) available. See DOI: https://doi.org/10.1039/d4ma00094c

dots,[21] tetrabutylammonium iodide,[22] phytic acid dipotassium,[23] graphdiyne oxide,[24] lead sulfide quantum dots,[25] poly(vinylpyrrolidone),[26] NH_4·Cl,[27] and tyrosine.[28] These functional additives not only modify SnO_2 ETLs to enhance the electron extraction and transport capabilities, but also passivate SnO_2 ETLs or/and ETL/perovskite interfaces for suppressing nonradiative charge recombination, which can eventually contribute to improving the crystal growth and quality of perovskite layers. Lee *et al.* incorporated oxidized black phosphorus quantum dots (O-BPs) into SnO_{2-x} to passivate oxygen vacancies in SnO_{2-x}, and thus unfavorable phase formation at $FAPbI_3/SnO_2$ interface was highly suppressed.[29] Wang *et al.* modified SnO_2 by using $CoCl_2·6H_2O$, leading to a favorable energy level alignment and a significant suppressed interfacial recombination at the ETL/perovskite interface.[30]

The rare earth element Ce has been used to dope TiO_2 ETLs to improve the performance of PSCs.[31–34] Chen *et al.* reported that Ce doping enlarged the band gap, upshifted the Fermi level, and reduced the surface defect density of the TiO_2 ETL, thus increasing the open-circuit voltage (V_{OC}) and final PCE of PSCs.[31] Ce ions are also incorporated into other functional layers within PSCs, such as perovskite films,[35,36] NiO_x hole transport layers,[37,38] and indium oxide transparent electrodes,[39] to enhance the efficiency of PSCs. However, doping of Ce ions into SnO_2 ETLs has not been reported yet.

Regarding the manufacturing process of these doped or modified SnO_2 ETLs, almost all the processes involved the use of spin coating which is not compatible with large-scale manufacturing of PSCs. There are only very few published reports focused on the scaling up of the fabrication of doped SnO_2 ETLs.[40] As a low-cost, waste-free, contactless, and maskless deposition method with digital control on printed patterns, inkjet printing has great potential for large-scale manufacturing of PSCs.[41] Herein, we modified SnO_x by Ce doping for use as ETLs, prepared through a scalable inkjet printing process. Compared with the pristine SnO_x, Ce-doped SnO_x showed increased conductivity and improved energy band alignment with the perovskite layer. Ce doping also passivated the surface defects of SnO_x. The photoluminescence results exhibited the suppression of the carrier recombination within the perovskite film upon Ce doping. We fabricated planar PSCs using Ce-doped SnO_x ETLs and achieved an improved PCE for the doped devices, compared to the undoped ones.

Results and discussion

To investigate the effects of Ce doping on the film quality and properties of the SnO_x thin films, SnO_x doped with various Ce concentrations was prepared *via* an inkjet printing process, and the physical properties were analyzed. Fig. 1a and b show the top-view scanning electron microscopy (SEM) images of pristine SnO_x and doped SnO_x with a Ce content of 2.5 at% (molar ratio of Ce to Sn ions). Other SEM images of 5 at%, 7.5 at%, and 10 at% Ce doped SnO_x are displayed in Fig. S1 (ESI†). Note that the large 100 nm-scale dome-shaped structures are the large grains of the FTO substrates under the SnO_x films (Fig. S1d, ESI†). The resulting pristine and doped SnO_x thin films were compact and dense with no pinholes. There was no obvious

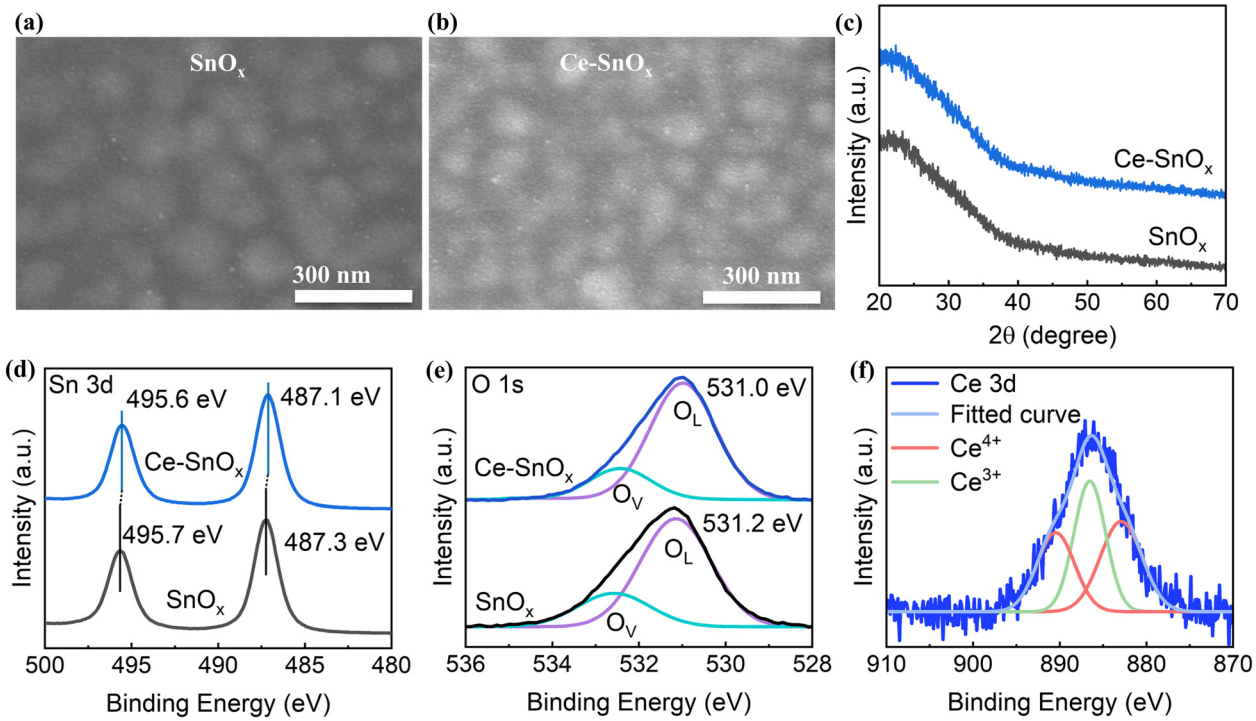

Fig. 1 (a) and (b) Top-view SEM images, (c) XRD patterns, (d) Sn 3d XPS, and (e) O 1s XPS spectra of pristine and 2.5 at% Ce-doped SnO_x. (f) Ce 3d XPS spectra of 2.5 at% Ce-doped SnO_x.

difference observed in the surface morphology between pristine SnO_x and Ce-doped SnO_x. X-ray diffraction (XRD) patterns were obtained for the pristine and doped SnO_x thin films, shown in Fig. 1c (and Fig. S2, ESI†). Both pristine and Ce-doped SnO_x showed an amorphous structure with no diffraction peaks detected. This is also the reason that the SEM surface images are lacking "crisp" well-defined features. The amorphous films have a smooth morphology without sharp features.

X-ray photoelectron spectroscopy (XPS) measurements were conducted to investigate the chemical states of pristine and Ce-doped SnO_x. As seen in the Sn 3d XPS spectrum of SnO_x (Fig. 1d), the two peaks at 495.7 eV and 487.3 eV were assigned to Sn $3d_{3/2}$ and Sn $3d_{5/2}$, respectively. The O 1s XPS spectrum of SnO_x exhibited a peak at 931.2 eV (Fig. 1e). Upon Ce doping, the peaks in both Sn 3d and O 1s spectra moved to lower binding energy regions, indicating a possible chemical interaction between Ce and SnO_x.[16,42] The results also suggested the presence of Sn^{4+} oxidation states in SnO_x and Ce doped SnO_x. The peak in the Ce 3d XPS spectrum was resolved into three components representing Ce^{3+} and Ce^{4+} oxidation states (Fig. 1f). This result confirmed that Ce ions were successfully incorporated into the host SnO_x lattice system. Furthermore, the O 1s XPS peak was deconvoluted into two peaks, one representing the lattice oxygen (O_L) in SnO_x and the other one originating from the oxygen vacancies or chemisorbed hydroxyl groups (O_V). As the Ce doping concentration increased from 0 to 2.5 at%, the ratio of O_V to total oxygen decreased from 24.11% to 19.40% (Table S1, ESI†). Thus, the surface oxygen defects of SnO_x were passivated upon introducing Ce ions, thereby reducing recombination losses at ETL/perovskite interfaces within PSCs.

The optical properties of pristine and Ce-doped SnO_x samples were also investigated by ultraviolet-visible (UV/Vis) absorption measurements. As displayed in Fig. 2a, the transmittance of both pristine and Ce-doped SnO_x was above 80% in the visible light region, which verified the transparency of pristine and Ce-doped SnO_x as ETLs for planar PSCs. The transmittance and absorption (Fig. S3, ESI†) changed slightly upon Ce doping. The Tauc's relationship was used to determine the optical band gap (E_g) of SnO_x and Ce-doped SnO_x, which is described using a formula:

$$(\alpha h\nu)^2 = C \times (h\nu - E_g) \quad (1)$$

where α, $h\nu$, and C are the optical absorption coefficient, the photon energy, and the material constant, respectively.[43] The two samples exhibited the same optical band gap of 3.76 eV (Fig. 2b). The ultraviolet photoelectron spectroscopy (UPS) measurements were performed to investigate the effect of Ce doping on the energy levels of SnO_x. The work function can be calculated using the equation:

$$E_F = 21.22 - (E_{onset} - E_{cutoff}) \quad (2)$$

where E_F refers to the Fermi level, E_{onset} and E_{cutoff} represent the onset and the cutoff of the UPS spectrum, respectively.

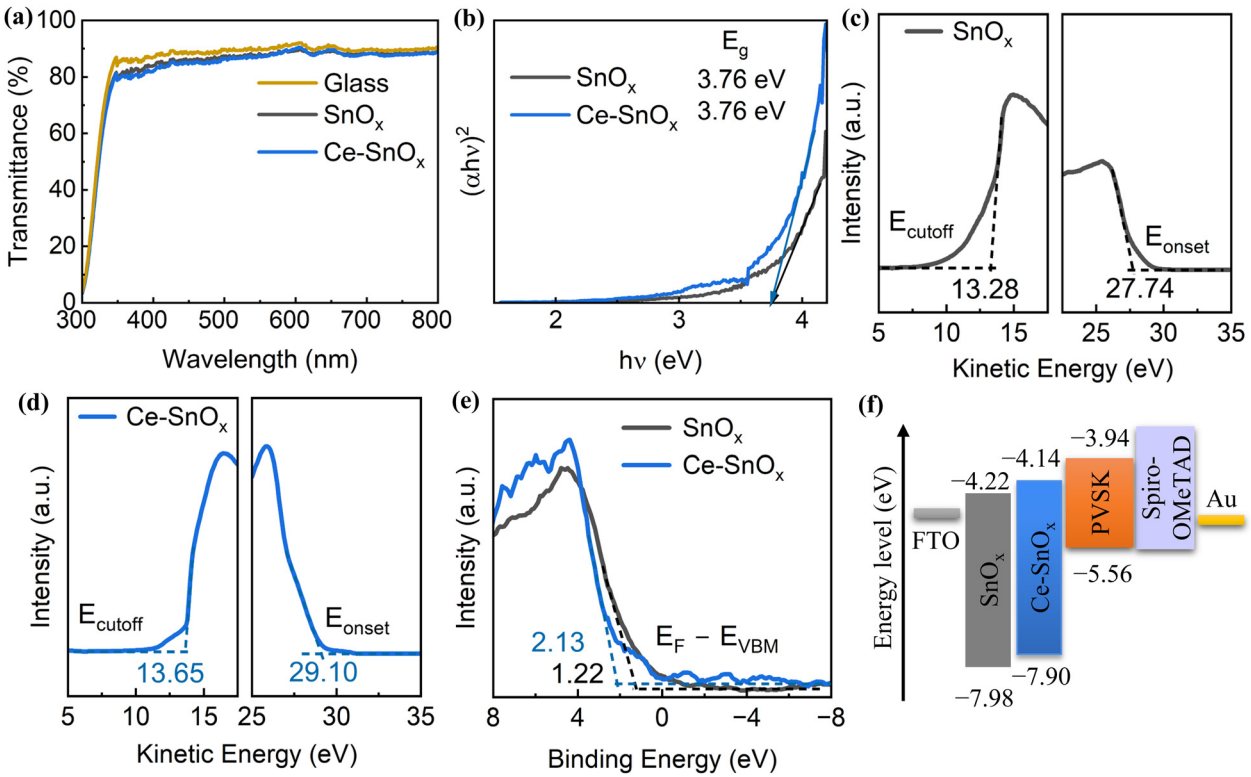

Fig. 2 (a) Transmittance, (b) Tauc's plots, (c) and (d) UPS spectra, and (e) valence band XPS spectra of pristine SnO_x and 2.5 at% Ce-doped SnO_x. (f) Energy band diagram of PSCs based on SnO_x and 2.5 at% Ce-doped SnO_x ETLs.

As shown in Fig. 2c and d, the work function was calculated to be 6.76 eV and 5.77 eV for SnO_x and Ce-doped SnO_x, respectively. From the valence band XPS spectra (Fig. 2e), the valence band maximum (E_{VBM}) of SnO_x and Ce-doped SnO_x was obtained to be 1.22 eV and 2.13 eV below the Fermi level and thus the values were calculated to be −7.98 eV and −7.90 eV, respectively. The conduction band minimum was then determined to be −4.22 eV and −4.14 eV using the formula $E_{CBM} = E_{VBM} + E_g$. The energy levels of the perovskite layer were obtained from the literature.[44] The consequent energy band diagram of PSCs with SnO_x and Ce-doped SnO_x ETLs was displayed in Fig. 2f. The observed decrease in work function from 6.76 eV in SnO_x to 5.77 eV in Ce-doped SnO_x indicates that Ce addition altered the local chemical environment of the Sn atoms, reducing their binding energy, which agrees with the observed slight shift of Sn (Fig. 1d). This phenomenon likely increased the electron density at the Sn sites, effectively lowering the energy required to remove an electron from the surface, which was reflected in the reduced work function. Therefore, the energy levels were upshifted upon Ce doping, and the conduction band minimum of Ce-doped SnO_x became closer to that of the perovskite layer than that of pristine SnO_x. This can enhance the electron extraction and reduce the recombination losses at ETL/perovskite interfaces, which is beneficial for improving the open-circuit voltage (V_{OC}).[16,18]

The electrical properties of pristine and Ce-doped SnO_x thin films were also studied. The conductivity of SnO_x increased at first and then decreased when the Ce doping concentration increased from 0 to 10 at% (Fig. S4, ESI†). The conductivity of 2.5 at% Ce-doped SnO_x was estimated to be 7.57×10^{-5} S cm^{-1} (Fig. 3a), which was about 2.6 times higher than that of pristine SnO_x (2.96×10^{-5} S cm^{-1}). This enhancement originated from the increase in the electron density as well as the passivation of the surface defects in SnO_x upon Ce doping.[42,45] The improved electrical conductivity of Ce-doped SnO_x can boost the charge transfer at ETL/perovskite interfaces, leading to improved short-circuit current density (J_{SC}). The steady-state photoluminescence (PL) and time-resolved photoluminescence (TRPL) measurements were performed to investigate the charge transfer dynamics and examine the perovskite film quality. The perovskite films deposited on Ce-doped SnO_x exhibited stronger PL intensities than that deposited on pristine SnO_x (Fig. 3b and Fig. S5, ESI†), which indicated that the carrier recombination in Ce–SnO_x/perovskite films was effectively suppressed.[46] This was further verified by the TRPL results (Fig. 3c). The TRPL decay curves were fitted with a bi-exponential decay function:

$$I(t) = A_1 \exp(-\frac{t}{\tau_1}) + A_2 \exp(-\frac{t}{\tau_2}) + I_0 \quad (3)$$

where τ_1 and τ_2 represent the fast and slow decay component, and A_1 and A_2 are the corresponding decay amplitude fractions, respectively. The average lifetime (τ_{ave}) was calculated by the formula $\tau_{ave} = A_1\tau_1 + A_2\tau_2$. The fitting parameters were summarized in Table S2 (ESI†). The fast decay (τ_1) could be assigned to the quenching process of photogenerated carriers transferring from the perovskite film through the ETL to the FTO electrode,

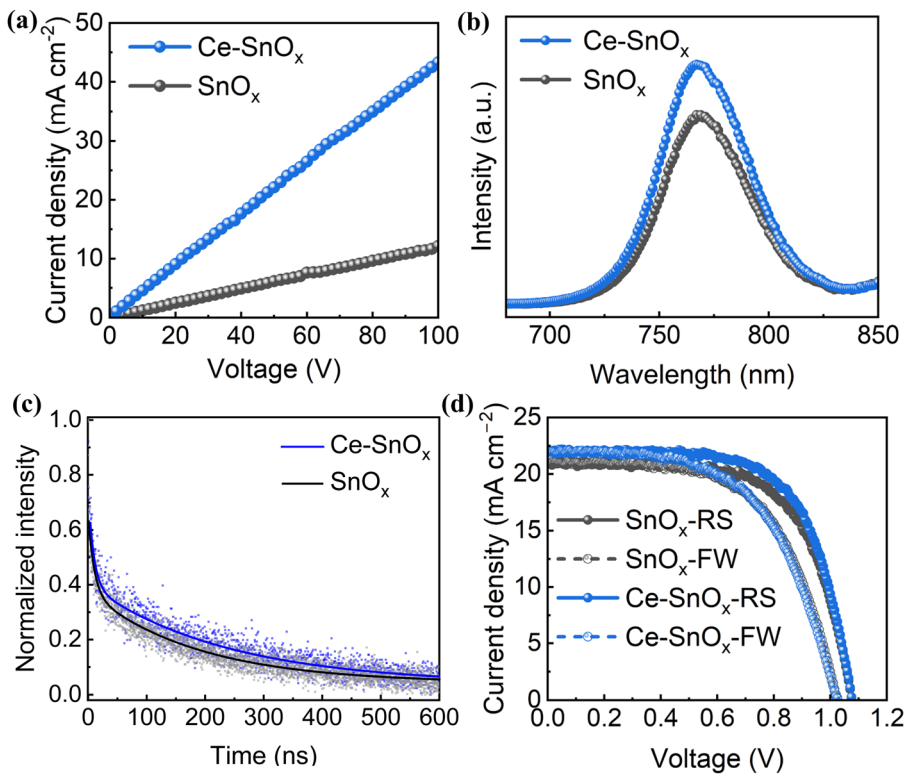

Fig. 3 (a) Current–voltage curves for calculating the conductivity of SnO_x and 2.5 at% Ce-doped SnO_x. (b) PL and (c) normalized TRPL spectra of FTO/SnO_x/perovskite and FTO/Ce–SnO_x/perovskite. (d) *J*–*V* characteristics of the cells with pristine SnO_x and 2.5 at% Ce-doped SnO_x ETLs.

Table 1 Photovoltaic parameters of PSCs with inkjet-printed pristine SnO_x and 2.5 at% Ce-doped SnO_x

ETL	Scan direction	PCE (%)	V_{OC} (V)	J_{SC} (mA cm^{-2})	FF (%)
SnO_x	reverse	14.66	1.08	20.96	65.0
2.5 at% Ce–SnO_x	reverse	15.77	1.08	21.98	66.4

and the slow decay (τ_2) could originate from the radiative recombination of free charge carriers in the perovskite film before the charge transfer.[47,48] The Ce–SnO_x/perovskite film showed increased fraction A_1, suggesting decreased non-radiative recombination, while the increased τ_2 from 188 ns to 236 ns upon Ce doping could indicate a decrease in the recombination of free carriers or a suppression of defects forming in the perovskite film.[49] The suppressed non-radiative recombination may originate from the improved perovskite crystallization or decreased defect density induced by the passivation of the oxygen defects on the Ce-doped SnO_x surface.[16]

PSCs with pristine and Ce-doped SnO_x ETLs were fabricated to study the effect of Ce doping on the device performance. The current density–voltage (J–V) curves and photovoltaic parameters, *i.e.*, V_{OC}, J_{SC}, fill factor (FF), and PCE are shown in Fig. 3d and Table 1, respectively. An optimum PCE of 15.77% was achieved for the cell with a 2.5 at% Ce-doped SnO_x ETL, higher than 14.66% for the cell with pristine SnO_x ETL. A significantly improved average PCE of 15.05 ± 0.58% was also delivered by the Ce-doped SnO_x (2.5 at%) ETLs compared to 13.87 ± 0.40% for pristine SnO_x ETLs (Table S3 and Fig. S6, ESI†), originating from the improvement in all three photovoltaic parameters V_{OC}, J_{SC}, and FF. The improved performance was attributed to enhanced electron extraction and transport and suppressed carrier recombination at ETL/perovskite interfaces, originating from reduced surface defects, enhanced conductivity, and improved energy band alignment between the ETL and the perovskite layer. Further optimization can be carried out to boost the efficiency to higher levels through optimizing each functional layer and interfaces within the PSC devices. The achieved efficiency of 15.77% is still competitive in comparison with the reported values of 13.08% and 18.8% realized by similar inkjet-printed SnO_2 ETLs.[50,51] In addition, this work provides some insights to ionic doping of SnO_x ETLs *via* a scalable inkjet printing method.

Conclusions

In summary, inkjet-printed Ce-doped SnO_x was successfully fabricated as an effective electron transport layer for planar PSCs. Ce-doped SnO_x showed enhanced conductivity and improved energy band alignment with the perovskite layer, contributing to facilitating charge extraction and transport capabilities. Upon Ce doping, the surface defects of SnO_x were also passivated. The photoluminescence characterization revealed that the perovskite film deposited on Ce-doped SnO_x exhibited a longer decay lifetime, representing the suppression of the carrier recombination within the perovskite film. Consequently, planar PSCs with Ce-doped SnO_x (2.5 at%) ETLs delivered an improved PCE of 15.77%, compared to those devices with undoped SnO_x ETLs (14.66%). Moreover, this work demonstrated a sustainable and scalable inkjet printing method for the fabrication of efficient planar PSCs.

Experimental

Materials

All chemicals were used as received without further modifications. Tin(IV) acetate ($Sn(CH_3CO_2)_4$) and cerium(III) nitrate hexahydrate ($Ce(NO_3)_3{\cdot}6H_2O$, 99.99%) were purchased from Sigma-Aldrich (Darmstadt, Germany). Lead iodide (PbI_2, 99.99%) and lead bromide ($PbBr_2$, >98.0%) were purchased from TCI (Tokyo, Japan). Formamidinium iodide (FAI, $CH(NH_2)_2I$, >98%) and methylammonium bromide (MABr, CH_3NH_3Br, >98%) were purchased from Dyenamo (Stockholm, Sweden) and Sigma-Aldrich (Darmstadt, Germany), respectively. Spiro-OMeTAD (99.8%) was purchased from Borun New Material Technology (Ningbo, China). Bis(trifluoromethane)sulfonimide lithium salt (LiTFSI, 99.95%), FK209 (Co(III) TFSI salt, 98%) and 4-*tert*-butylpyridine (TBP, 98%) were obtained from Sigma-Aldrich (Darmstadt, Germany).

Set-up of inkjet printer

A piezoelectric drop-on-demand inkjet system was designed for the printheads from XaarJet in our lab.[52,53] Inkjet printing of pristine and Ce-doped SnO_x thin films was performed under ambient conditions by employing XJ126/80 printheads which possess 126 active nozzles and can yield a drop volume of 80 pL. A customized waveform was used to form and eject droplets. The printing frequency was set as 283.46 Hz, and the printing resolution was 360 dpi.

Inkjet printing of pristine and Ce-doped SnO_x thin layers

The ink for printing SnO_x thin films was prepared by dissolving tin(IV) acetate in a mixture of 2-propanol and propylene glycol (9/1, v/v) to form a 0.05 M precursor solution. A small amount of ethanolamine was added to improve the acetate solubility. The precursor ink was then inkjet-printed onto substrates which were pre-heated at 60 °C. The as-printed thin films were dried at 60 °C for 5 min and afterwards were annealed inside a furnace at 220 °C for 1 h. Ce-doped SnO_x thin films were fabricated in a similar process to pristine SnO_x thin films. The only difference lied in the preparation of the precursor ink. A certain amount of a 0.25 M $Ce(NO_3)_3$ solution, consisting of $Ce(NO_3)_3{\cdot}6H_2O$ dissolved in a mixture of 2-propanol and propylene glycol (9/1, v/v), was added to a 0.05 M tin acetate solution prepared as described above. The amount of the added $Ce(NO_3)_3$ solution was determined based on the desired doping level, *e.g.*, 50 μL for 2.5 at%. Then, the mixed solution was used for inkjet printing of Ce-doped SnO_x thin films. The inkjet printing and post-treatment processes were the same as the fabrication process of pristine SnO_x thin films.

Device fabrication

FTO glass substrates (13 Ω sq^{-1}, Sigma–Aldrich) were cut into pieces with the dimension of 25 × 15 mm. Each piece was

etched at the edge through dripping 2 M HCl aqueous solution onto Zn powder. These substrates were successively sonicated in a detergent solution (5% deconex in water), deionized water, acetone, and 2-propanol for 15 min. Before inkjet printing, FTO substrates were pre-heated at 500 °C for 30 min and afterwards cooled down to room temperature. Compact SnO_x or Ce-doped SnO_x ETLs were fabricated *via* inkjet printing as described above. Then, the perovskite layers were fabricated following the procedure reported previously.[54] The perovskite precursor was prepared by dissolving PbI_2, FAI, $PbBr_2$, and MABr in a mixed solvent (*N*,*N*-dimethylformamide/dimethyl sulfoxide = 4/1, v/v) to form a 1.3 M Pb precursor solution. The molar ratio of PbI_2/FAI/$PbBr_2$/MABr was 1.1/1/0.2/0.2. Seventy-five μL of the perovskite precursor was spin-coated at 4500 rpm for 30 s. During the spin coating, 125 μL of chlorobenzene was dripped onto the perovskite film at 15 s. The as-deposited perovskite film was immediately dried at 100 °C for 30 min. A hole transport layer was spin-coated at 4000 rpm for 30 s with a precursor consisting of 85.8 mg Spiro-OMeTAD, 35 μL LiTFSI solution (0.6 M), 33.8 μL TBP, and 10 μL FK 209 solution (0.2 M) dissolved in 1 mL chlorobenzene. Finally, an 80 nm-thick Au electrode was thermally evaporated (Edwards Auto 306) onto the substrates.

Characterization

The morphology of the pristine and Ce-doped SnO_x thin films was studied using a combined focused ion beam/scanning electron microscope (FIB/SEM, FEI Nova 600 Nanolab, FEI Company, Eindhoven, The Netherlands). XRD patterns were obtained employing an X-ray diffractometer (Siemens D5000, Siemens, Munich, Germany) with a Cu Kα radiation (λ = 1.5406 Å). The XPS and UPS measurements were conducted using the K-alpha XPS/UPS system manufactured by Thermo Scientific. For XPS analysis, the spectra were obtained using a monochromatized Al Kα line with a photon energy ($h\nu$) of 1486.6 eV. For UPS analysis, a He1 ultraviolet light source with an energy of 21.22 eV was employed. The valence band photoelectron signal originated from the top 2–3 nm of the sample's surface, and the electronic work function of the material's surface was measured. The UV/Vis absorption and transmittance spectra were obtained using a Lambda 750 spectrophotometer. The conductivity of thin films was measured according to the report[55] and the details of the measurement were shown in Fig. S7 (ESI†). Current–voltage (*I–V*) characteristics were collected using a Keithley 2400 instrument. The steady-state PL of perovskite films was investigated using Fluorolog FL 3-22 spectrometer at room temperature (Horiba Jobin Yvon, Longjumeau, France), equipped with a double excitation monochromator, a single emission monochromator (HR320) and a R928P PMT detector. A continuous xenon lamp (450 W) was used for steady state measurements. A supercontinuum laser (Fianium WhiteLase) was employed as a source for the TRPL. For all photoluminescence measurements the excitation wavelength was 500 nm, and the detection wavelength was 765 nm. The active area of the solar cells was defined by a mask of 0.152 cm^2 and was illuminated under an AM 1.5 G solar simulator (Newport 91160-1000) with an incident light density of 100 mW cm^{-2}. *J–V* characteristics of the PSC devices were recorded at a scan rate of 125 mV s^{-1}, using a Keithley 2400 unit.

Data availability

The data supporting this article have been included as part of the ESI.†

Conflicts of interest

There are no conflicts to declare.

Acknowledgements

The authors sincerely acknowledge the valuable discussions with Dr. Jinghua Guo and Dr. Feipeng Yang. This research was funded by China Scholarship Council (No. 201700260217) and Jernkontoret (Stiftelsen Jernkontorsfonden för Bergsvetenskaplig Forskning and Stiftelsen Prvtziska fonden nr 2). Work at the Molecular Foundry was supported by the Office of Science, Office of Basic Energy Sciences, of the U. S. Department of Energy under Contract No. DE-AC02-05CH11231. JG and MJ gratefully acknowledge the support of the Swedish government through the strategic research area STandUP for ENERGY and from Energimyndigheten (Swedish Energy Agency, grant number: 49278-1).

References

1 S. Y. Park and K. Zhu, *Adv. Mater.*, 2022, **34**, 2110438.
2 Q. Jiang, L. Zhang, H. Wang, X. Yang, J. Meng, H. Liu, Z. Yin, J. Wu, X. Zhang and J. You, *Nat. Energy*, 2016, **2**, 16177.
3 D. Richards, D. Burkitt, R. Patidar, D. Beynon and T. Watson, *Mater. Adv.*, 2022, **3**, 8588–8596.
4 K. Wei, J. Deng, L. Yang, C. Zhang, M. Huang, X. Cai, X. Zhang and J. Zhang, *Adv. Energy Mater.*, 2023, **13**, 2203448.
5 J. Tian, J. Wu, R. Li, Y. Lin, J. Geng, W. Lin, Y. Wang, Q. Ouyang, Z. Wu, W. Sun, L. Li, Z. Lan and Y. Lin, *Nano Energy*, 2023, **118**, 108939.
6 L. Zhang, C. Fu, S. Wang, M. Wang, R. Wang, S. Xiang, Z. Wang, J. Liu, H. Ma, Y. Wang, Y. Yan, M. Chen, L. Shi, Q. Dong, J. Bian and Y. Shi, *Adv. Funct. Mater.*, 2023, **33**, 2213961.
7 H. Ye, Z. Liu, X. Liu, B. Sun, X. Tan, Y. Tu, T. Shi, Z. Tang and G. Liao, *Appl. Surf. Sci.*, 2019, **478**, 417–425.
8 P. Sakthivel, S. Foo, M. Thambidurai, P. C. Harikesh, N. Mathews, R. Yuvakkumar, G. Ravi and C. Dang, *J. Power Sources*, 2020, **471**, 228443.
9 X. Zhou, W. Zhang, X. Wang, P. Lin, S. Zhou, T. Hu, L. Tian, F. Wen, G. Duan, L. Yu, Y. Xiang, B. Huang and Y. Huang, *Appl. Surf. Sci.*, 2022, **584**, 152651.
10 H. Chen, D. Liu, Y. Wang, C. Wang, T. Zhang, P. Zhang, H. Sarvari, Z. Chen and S. Li, *Nanoscale Res. Lett.*, 2017, **12**, 238.

11 Z. Ma, W. Zhou, Z. Xiao, H. Zhang, Z. Li, J. Zhuang, C. Peng and Y. Huang, *Org. Electron.*, 2019, **71**, 98–105.
12 J. Song, W. Zhang, D. Wang, K. Deng, J. Wu and Z. Lan, *Sol. Energy*, 2019, **185**, 508–515.
13 Y. Bai, Y. Fang, Y. Deng, Q. Wang, J. Zhao, X. Zheng, Y. Zhang and J. Huang, *ChemSusChem*, 2016, **9**, 2686–2691.
14 G. Yang, H. Lei, H. Tao, X. Zheng, J. Ma, Q. Liu, W. Ke, Z. Chen, L. Xiong, P. Qin, Z. Chen, M. Qin, X. Lu, Y. Yan and G. Fang, *Small*, 2017, **13**, 1601769.
15 M. Park, J.-Y. Kim, H. J. Son, C.-H. Lee, S. S. Jang and M. J. Ko, *Nano Energy*, 2016, **26**, 208–215.
16 R. Wang, J. Wu, S. Wei, J. Zhu, M. Guo, Q. Zheng, M. Wei and S. Cheng, *J. Power Sources*, 2022, **544**, 231870.
17 X. Ren, D. Yang, Z. Yang, J. Feng, X. Zhu, J. Niu, Y. Liu, W. Zhao and S. F. Liu, *ACS Appl. Mater. Interfaces*, 2017, **9**, 2421–2429.
18 Y. W. Noh, J. H. Lee, I. S. Jin, S. H. Park and J. W. Jung, *Nano Energy*, 2019, **65**, 104014.
19 W. Cao, J. Zhang, K. Lin, L. Qiu, J. Li, Y. Dong, J. Wang, D. Xia, R. Fan and Y. Yang, *Sol. RRL*, 2021, **5**, 2100058.
20 C. Wang, J. Wu, X. Liu, S. Wang, Z. Yan, L. Chen, G. Li, X. Zhang, W. Sun and Z. Lan, *J. Alloys Compd.*, 2021, **886**, 161352.
21 B. Gu, Y. Du, B. Chen, R. Zhao, H. Lu, Q. Xu and C. Guo, *ACS Appl. Mater. Interfaces*, 2022, **14**, 11264–11272.
22 H. Wang, J. Yuan, J. Xi, J. Du and J. Tian, *J. Phys. Chem. Lett.*, 2021, **12**, 9142–9148.
23 C. Liu, M. Guo, H. Su, P. Zhai, K. Xie, Z. Liu, J. Zhang, L. Liu and H. Fu, *Appl. Surf. Sci.*, 2022, **588**, 152943.
24 L. Yao, M. Zhao, L. Liu, S. Chen, J. Wang, C.-J. Zhao, Z. Jia, S. Pang, X. Guo and T. Jiu, *Mater. Chem. Front.*, 2021, **5**, 6913–6922.
25 L. He, H. Su, Z. Li, H. Liu and W. Shen, *Adv. Funct. Mater.*, 2023, **33**, 2213963.
26 D. Wang, S.-C. Chen and Q. Zheng, *J. Mater. Chem. C*, 2019, **7**, 12204–12210.
27 J. Liang, Z. Chen, G. Yang, H. Wang, F. Ye, C. Tao and G. Fang, *ACS Appl. Mater. Interfaces*, 2019, **11**, 23152–23159.
28 C. Yu, B. Zhang, G. Wang, J. Wang, J. Zhang, P. Chen, C. Li and Y. Duan, *Appl. Phys. Lett.*, 2022, **121**, 073501.
29 J. H. Lee, S. Lee, T. Kim, H. Ahn, G. Y. Jang, K. H. Kim, Y. J. Cho, K. Zhang, J.-S. Park and J. H. Park, *Joule*, 2023, **7**, 380–397.
30 P. Wang, B. Chen, R. Li, S. Wang, N. Ren, Y. Li, S. Mazumdar, B. Shi, Y. Zhao and X. Zhang, *ACS Energy Lett.*, 2021, **6**, 2121–2128.
31 K. Chen, H. Zhang, H. Tong, L. Wang, L. Tao, K. Wang, Y. Zhang and X. Zhou, *Int. J. Hydrogen Energy*, 2021, **46**, 5677–5688.
32 J. Jin, H. Li, W. Bi, C. Chen, B. Zhang, L. Xu, B. Dong, H. Song and Q. Dai, *Sol. Energy*, 2020, **198**, 187–193.
33 H. Lu, J. Zhuang, Z. Ma, W. Zhou, H. Xia, Z. Xiao, H. Zhang and H. Li, *RSC Adv.*, 2019, **9**, 1075–1083.
34 R. Xu, Y. Li, S. Feng, J. Wang, J. Zhang, X. Zhang, C. Bian, W. Fu, Z. Li and H. Yang, *J. Mater. Sci.*, 2020, **55**, 5681–5689.
35 Z. Song, W. Xu, Y. Wu, S. Liu, W. Bi, X. Chen and H. Song, *Small*, 2020, **16**, 2001770.
36 D. Hu, H. Tang, X. Zhang, Z. Li, X. Zhu and T. Zhu, *Sol. RRL*, 2023, **7**, 2201129.
37 K. Zhao, Y. Zhao, Y. Tan, K. Hu and Z.-S. Wang, *ACS Appl. Energy Mater.*, 2021, **4**, 9038–9045.
38 F. P. Gokdemir Choi, H. Moeini Alishah and S. Gunes, *Appl. Surf. Sci.*, 2021, **563**, 150249.
39 S. An, P. Chen, F. Hou, Q. Wang, H. Pan, X. Chen, X. Lu, Y. Zhao, Q. Huang and X. Zhang, *Sol. Energy*, 2020, **196**, 409–418.
40 E. Halvani Anaraki, A. Kermanpur, M. T. Mayer, L. Steier, T. Ahmed, S.-H. Turren-Cruz, J. Seo, J. Luo, S. M. Zakeeruddin, W. R. Tress, T. Edvinsson, M. Grätzel, A. Hagfeldt and J.-P. Correa-Baena, *ACS Energy Lett.*, 2018, **3**, 773–778.
41 B. Parida, A. Singh, A. K. Kalathil Soopy, S. Sangaraju, M. Sundaray, S. Mishra, S. Liu and A. Najar, *Adv. Sci.*, 2022, **9**, 2200308.
42 Y. Wang, Y. Li, C. Li, C. Wang, Q. Zhou, L. Liang, Z. Zhang, C. Liu, W. Yu, X. Yu and P. Gao, *Small*, 2024, 2402531.
43 J. Tauc and A. Menth, *J. Non-Cryst. Solids*, 1972, **8–10**, 569–585.
44 S. Song, G. Kang, L. Pyeon, C. Lim, G.-Y. Lee, T. Park and J. Choi, *ACS Energy Lett.*, 2017, **2**, 2667–2673.
45 P. S. Archana, A. Gupta, M. M. Yusoff and R. Jose, *Appl. Phys. Lett.*, 2014, 105.
46 Q. Jiang, Y. Zhao, X. Zhang, X. Yang, Y. Chen, Z. Chu, Q. Ye, X. Li, Z. Yin and J. You, *Nat. Photonics*, 2019, **13**, 460–466.
47 Y. Li, L. Meng, Y. Yang, G. Xu, Z. Hong, Q. Chen, J. You, G. Li, Y. Yang and Y. Li, *Nat. Commun.*, 2016, **7**, 10214.
48 J. Fu, J. Zhang, T. Zhang, L. Yuan, Z. Zhang, Z. Jiang, Z. Huang, T. Wu, K. Yan, L. Zhang, A. Wang, W. Ji, Y. Zhou and B. Song, *ACS Nano*, 2023, **17**, 2802–2812.
49 F. Cai, J. Lin, W. Pan, S. Zhu, W. Li, Y. Du, J. Liu, M. Yang and J. Wu, *ACS Appl. Energy Mater.*, 2022, **5**, 8501–8509.
50 A. H. Ghahremani, D. Ratnayake, A. Sherehiy, D. O. Popa and T. Druffel, *Energy Technol.*, 2021, **9**, 2100452.
51 V. Rohnacher, F. Ullrich, H. Eggers, F. Schackmar, S. Hell, A. Salazar, C. Huck, G. Hernandez-Sosa, U. W. Paetzold, W. Jaegermann and A. Pucci, *Adv. Mater. Technol.*, 2021, **6**, 2000282.
52 M. Fang, Doctoral thesis, KTH Royal Institute of Technology, 2012.
53 Y. Wu, Doctoral thesis, KTH Royal Institute of Technology, 2010.
54 W. Zhang, P. Liu, A. Sadollahkhani, Y. Li, B. Zhang, F. Zhang, M. Safdari, Y. Hao, Y. Hua and L. Kloo, *ACS Omega*, 2017, **2**, 9231–9240.
55 C. Chen, W. Zhang, J. Cong, M. Cheng, B. Zhang, H. Chen, P. Liu, R. Li, M. Safdari, L. Kloo and L. Sun, *ACS Energy Lett.*, 2017, **2**, 497–503.